Journal of Alloys and Compounds 795 (2019) 385–390

Contents lists available at ScienceDirect

Journal of Alloys and Compounds

journal homepage: http://www.elsevier.com/locate/jalcom

First principles investigation of Be_3X_2 (X = N, P, As) and their alloys for solar cell applications

Mazhar Ullah [a, b, *], Roshan Ali [c], G. Murtaza [b], Yue Chen [a]

[a] Department of Mechanical Engineering, The University of Hong Kong, Pokfulam Road, Hong Kong, China
[b] Materials Modeling Lab, Department of Physics, Islamia College Peshawar, Pakistan
[c] The Guo China-US Photonics Laboratory, State Key Laboratory of Applied Optics, Changchun Institute of Optics, Fine Mechanics and Physics, Chinese Academy of Sciences, Changchun 130033, China

ARTICLE INFO

Article history:
Received 16 February 2019
Received in revised form
29 April 2019
Accepted 2 May 2019
Available online 3 May 2019

Keywords:
Beryllium nitride alloys
Optical spectra
Device absorption efficiencies

ABSTRACT

The ground state electronic structure and absorption efficiency of α-Be_3X_2 (X = N, P or As) and their alloys are investigated using density functional theory. All pristine compounds and alloys are found to have direct band gaps at the zone center Γ point. The $Be_{24}P_xN_{16-x}$ and $Be_{24}As_xN_{16-x}$ alloys (x = 4, 8, 12, or 16) are predicted to have suitable band gaps for solar absorber applications. The majority interband electronic transitions in the pristine compounds and the alloys are between the valence band *p*-states of N, P and As and the conduction band *p*-states of Be. The alloy systems show strong and wide absorption spectra, suggesting potential solar energy conversion applications.

1. Introduction

Much progress has been made recently in the research of binary nitrides and phosphides of the group IIA and IIB elements (Be, Mg, Ca, Zn and Cd). The II-V group semiconductors have a broad range of applications in the electronic and optoelectronic devices, such as solar cells, detectors and ultrasonic multipliers [1–3]. Particularly the nitrides and phosphides of Be, Mg and Zn are the major focus of interest and are being explored for the technological applications in optoelectronics, infrared (IR) sensors, solar cells and Hall generators [1,4,5]. Recent attention in the development of wide band gap as well as small band gap binary materials II_3–V_2 is due to their potential applications in optical devices [6–9].

Materials with direct band gaps above 4 eV may be used in optical devices in the ultra-violet (UV) region for a wide range of electro-optical and high temperature applications [10], while materials with direct band gaps below 3 eV may be used in optical devices in the visible and IR regions for potential applications, such as solar cells, sensors and detectors [11]. Among them Be_3N_2 is also stimulated by the demand for optical devices, such as light emitting diode and laser diode operating in the near UV region [12]. Additionally, the organic-inorganic perovskites were reported in 2009 for the first time as light absorbers in solar cells, with efficiencies of 3.1%–3.8% [13]. In addition the alkaline earth metal Be and Mg also forms small and direct band gap semiconductors with group V elements, which are promising for thermoelectric applications [14–16].

Herein, we focus on beryllium (Be) nitride (N), beryllium phosphide (P) and beryllium arsenide (As) semiconductors and their alloys. It was reported that α-Be_3X_2 (X = N, P or As) has a cubic crystal structure with 40 atoms per unit cell [17] and β-Be_3X_2 has a hexagonal structure with 10 atoms per unit cell [18]. It was found that β-Be_3X_2 can be obtained by heating α-Be_3X_2 to 1400 °C [10]. Moreover, these compounds may also exist in a tetragonal phase having 80 atoms per unit cell [19], or in a high pressure trigonal phase (Υ-Be_3X_2) [20] containing 5 atoms per unit cell. Among these compounds, α is the stable phase under ambient condition, while β is the high-temperature phase and Υ is the high-pressure phase. The focus of the present study is mainly on the α-Be_3X_2 compounds and their alloys.

The crystal structure of α-Be_3N_2 and its optical band gap were determined by Reckewega et al. [21] using X-ray powder diffraction data for structure analysis and diffuse IR reflectance spectroscopy for optical band gap measurements. Armanta et al. [12] calculated the structural and electronics properties of α-Be_3N_2 by performing all-electron ab-initio calculations using the Hartree-Fock (HF)

* Corresponding author. Department of Mechanical Engineering, The University of Hong Kong, Pokfulam Road, Hong Kong, China.
E-mail address: murtaza@icp.edu.pk (M. Ullah).

https://doi.org/10.1016/j.jallcom.2019.05.017
0925-8388/

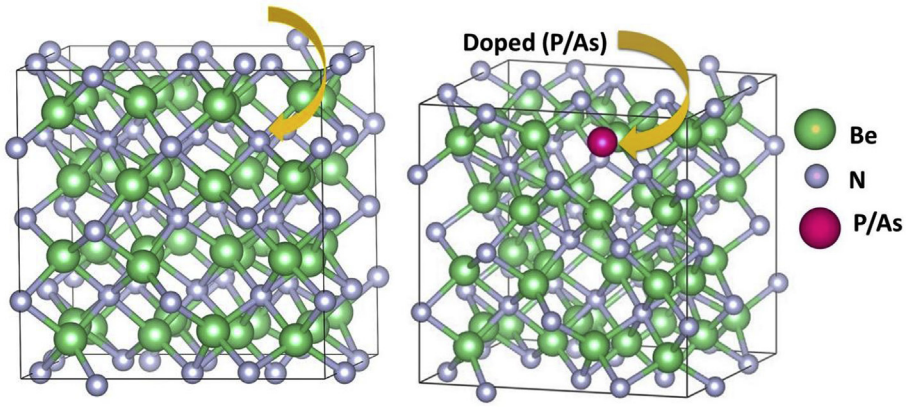

Fig. 1. Crystal structure of α-Be_3N_2 (left) and a schematic of the substitution of N by P/As (right).

approach. Eckerlin et al. [22] determined the crystal structure of β-Be_3X_2 by single crystal X-ray diffraction after the transformation from cubic to hexagonal phase at 1400 °C. The electronic structures of the high-temperature β-phase of these compounds were studied theoretically by Reyes-Serrato et al. [18] using all-electron HF method. Mokhtari et al. [10] also carried out theoretical calculations on the structural and electronic properties of β-Be_3N_2 by employing the pseudopotential plane wave (PP-PW) and the full potential linearized augmented plane wave (FP-LAPW) methods. Chang et al. [23] reported the structural, mechanical and the anisotropic nature of β-Be_3N_2 under high pressures based on first-principles calculations. Recently, the electronic structure and optical properties of the β-phase of beryllium nitride were calculated by Zarmiento-Garcia et al. [24] using WIEN2K program. The electronic and structural properties of the high-pressure γ-phase of these compounds were explored by Paliwal et al. [20] using the linear combination of atomic orbitals (LCAO) method; they suggested that the γ-phase is highly anisotropic with respect to momentum density distribution. The crystal structure of the tetragonal phase of Be_3P_2 was studied by Maslout et al. [19] based on X-ray and neutron diffractions. The pressure-induced phase transition from cubic to tetragonal Be_3P_2 was studied by Joshi et al. [25] using the LCAO methods implemented in the Crystal code.

It is cleared from the literature that only the structural and electronic properties of Be_3X_2 have been studied. Although there is a study of the optical properties of the β-phase of Be_3P_2, there is no complete information of the optical properties of these compounds and their alloys. This work presents the structural, electronic and optical properties of ground-state α-Be_3X_2 (X = N, P or As) under one umbrella. Moreover, this work is extended to the enhancement of device absorption efficiency by considering the effects of alloying.

2. Computational details

Density functional theory (DFT), implemented in the Vienna ab initio simulation package (VASP) [26], was used for the present calculations. Perdew-Burke-Ernzerhof (PBE) [27] generalized gradient approximation was used for structural optimization and electronic structure calculation. For more accurate band gap prediction, the Modified Beck and Johnson (mBJ) [28] approximation has been applied. In this study, we focused on the cubic phase of Be_3X_2 (X = N, P or As) with space group $Ia\bar{3}$ (#206) because it is stable at ambient temperature. The cubic phase of Be_3N_2 contains 40 atoms per primitive unit cell, in which there are 16 N atoms. For alloys, N atoms are replaced by P/As with different ratios as shown in Fig. 1. The alloy systems were simulated using the generalized quasirandom structures generated by minimizing the structural

Table 1
Total energies of different phases of Be_3X_2 (X = N, P or As) and the lattice constants of cubic Be_3X_2 compounds.

Compounds	Space group	Atoms/unit cell	Energy (eV/atom)	Lattice parameter (Å)		
				This calculation	Exp.	Other calculations
Be_3N_2	$Ia\bar{3}$	80	−6.67	8.15	8.145[a]	8.144[c]
Be_3N_2	$I4_1/acd$	160	−6.58			
Be_3N_2	$P6_3/mmc$	10	−6.63			
Be_3N_2	$P\bar{3}m1$	5	−6.45			
Be_3P_2	$Ia\bar{3}$	80	−4.65	10.19	10.15[b]	10.18[d], 10.17[e], 10.19[f]
Be_3P_2	$I4_1/acd$	160	−4.57			
Be_3P_2	$P6_3/mmc$	10	−4.58			
Be_3P_2	$P\bar{3}m1$	5	−4.53			
Be_3As_2	$Ia\bar{3}$	80	−4.18	10.65	–	–
Be_3As_2	$I4_1/acd$	160	−4.10			
Be_3As_2	$P6_3/mmc$	10	−4.11			
Be_3As_2	$P\bar{3}m1$	5	−4.07			

[a] Ref. [21].
[b] Ref. [25].
[c] Ref. [12].
[d] Ref. [11] PBE-GGA.
[e] Ref. [11] Hybrid.
[f] Ref. [11] FP-LAPW.

order with the evolutionary algorithm, as implemented in Universal Structure Predictor: Evolutionary Xtallography (USPEX) [29]. All systems have been fully optimized before the calculations of electronic structures. A cut-off energy of 550 eV for the plane wave basis set was applied. For self-consistent and optical property calculations, a $6 \times 6 \times 6$ k-point mesh was used.

We applied PBE functional for the dielectric function and absorption coefficient calculations, and the scissor operator to achieve the projected optical absorption spectra. The absorption coefficients of these alloys are important for the study of light absorption. Furthermore, we also carried out device performance simulation of these alloys in which P/As were used as the substitutional atoms. The advantage of this device simulation is that, the absorption efficiency can be obtained directly and may be compared to future experiments. We compared the total device absorption efficiency of the parent materials and their alloys for better understanding of the PV performance. For absorption efficiency, real (ε_1) and imaginary (ε_2) parts of the dielectric function are calculated using the following equations.

$$\varepsilon_1(\omega) = 1 + \frac{2}{\pi} P \int \frac{\omega' \varepsilon_2(\omega')}{\omega'^2 - \omega^2} d\omega' \quad (1)$$

$$\varepsilon_2(\omega) = \frac{8}{2\pi\omega^2} \sum_{nn'}' \int |p_{nn'}(k)|^2 \frac{ds_k}{\nabla \omega_{nn'(k)}} \quad (2)$$

The real and imaginary parts are further used to obtain the refractive index (n) and extinction coefficient (k) by using the equations given below.

$$n = \frac{1}{\sqrt{2}} \left(\varepsilon_1 + \left(\varepsilon_1^2 + \varepsilon_2^2 \right)^{\frac{1}{2}} \right)^{\frac{1}{2}} \quad (3)$$

$$k = \frac{1}{\sqrt{2}} \left(-\varepsilon_1 + \left(\varepsilon_1^2 + \varepsilon_2^2 \right)^{\frac{1}{2}} \right)^{\frac{1}{2}} \quad (4)$$

Finally, we are able to obtain the device absorption efficiency using the refractive index and extinction coefficient.

3. Results and discussion

3.1. Stability of Be_3X_2 and its alloys

The phase stability of Be_3X_2 binary compounds is directly related to their electronic and photovoltaics (PV) performances. The formation energies of the different phases of Be_3X_2 compounds are given in Table 1. It is seen that α-Be_3X_2 (cubic $Ia\bar{3}$ #206) has the lowest energy and is the most stable phase compared to the

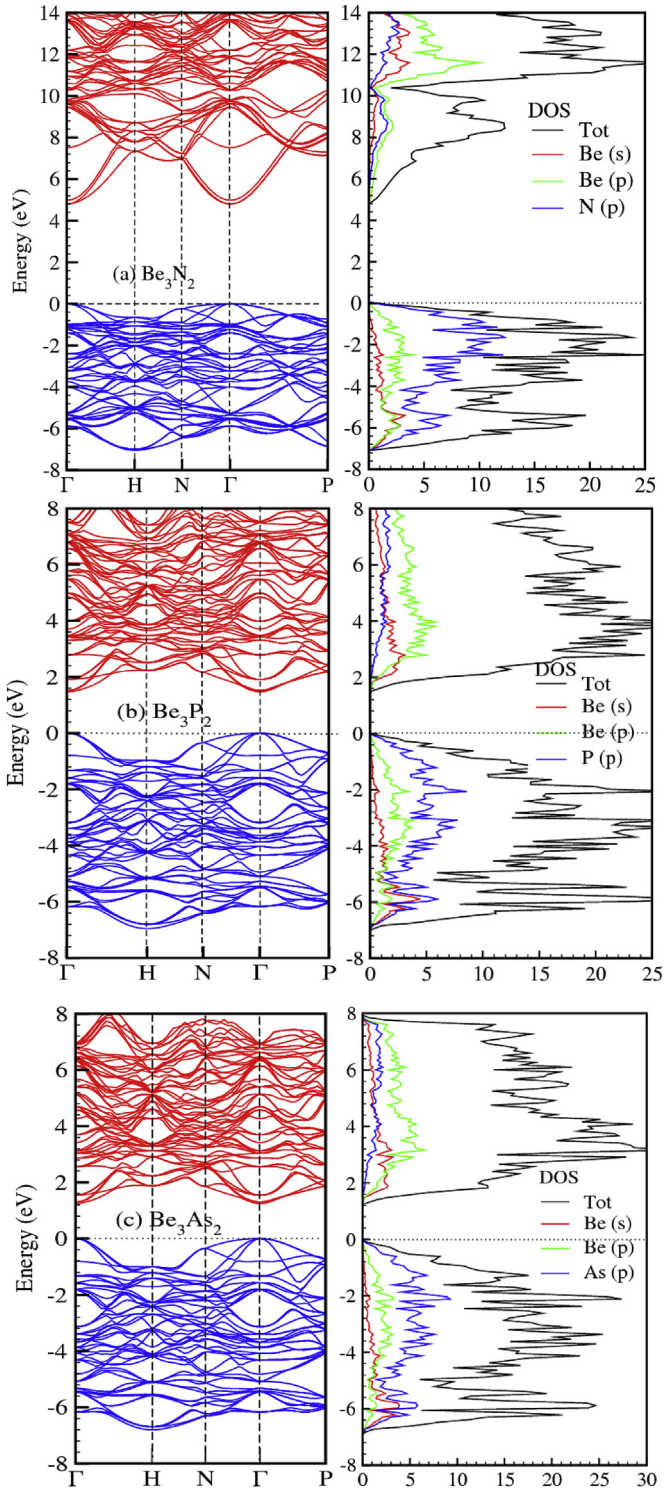

Fig. 2. Band structure and DOS of pristine Be_3X_2 (X = N, P or As) with space group $Ia\bar{3}$ (#206) calculated using the mBJ method.

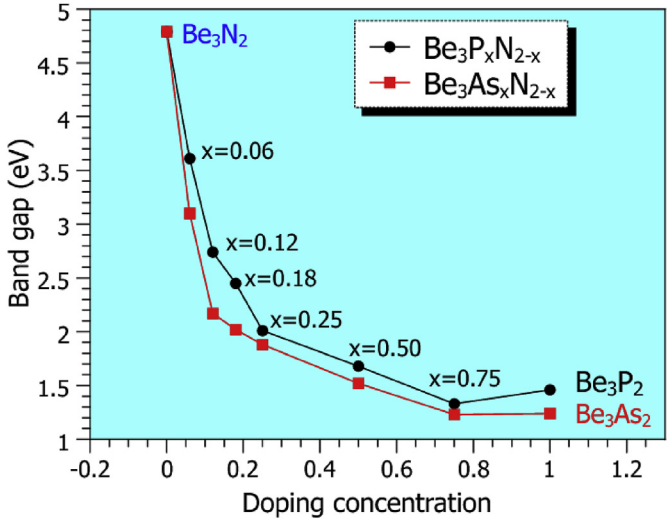

Fig. 3. Band gap of Be_3N_2 with different alloying concentrations of P/As calculated using the mBJ method. Here x shows the atomic alloying concentration.

hexagonal $P6_3/mmc$ (#194), trigonal $P\bar{3}m1$ (#164) and tetragonal $I4_1/acd$ (#142) phases. Other phases such as $P6_3/mmc$ and $P\bar{3}m1$ may become stable at high temperature [18] and high pressure [20], respectively. The primitive unit cell of cubic Be_3X_2 has a space group of $Ia\bar{3}$ (#206) and contains 40 atoms (24-Be and 16-N, P or As); it adopts an anti-bixbyite crystal structure as shown in Fig. 1. Beryllium atoms occupy the position 48e (x, y, z), while the X (N, P or As) atoms have two different crystallographic positions X_1 and X_2. Generally, X_1 atoms are located at positions 8b (0.25, 0.25, 0.25) and X_2 atoms occupy the positions 24d (u, 0, 0.25). The N atoms are replaced by P/As (denoted by red spheres) to obtain alloy systems ($Be_{24}P_xN_{16-x}$ or $Be_{24}As_xN_{16-x}$) for potential optoelectronic device applications. The lattice parameters and ground state energies of the parent compounds are obtained after full optimizations of the unit cells. The lattice constants of cubic Be_3N_2 and Be_3P_2 are 8.15 Å and 10.19 Å, respectively, in good agreement with the experimental values [21,25].

3.2. Electronic properties

The electronic and optoelectronic properties of materials are closely related to the band structure and density of state. In the present study, mBJ approximation is used for more accurate prediction of the electronic band gaps of Be_3X_2 and their alloys. The band structures of pristine compounds are shown in Fig. 2 (left panel). It is seen that Be_3X_2 (X = N, P or As) are direct band gap materials, where the conduction band minima and valence band maxima lie at the same Γ point in the Brillion zone. The band gaps of these semiconductors decrease as one stirs down from N to As. Moreover, Be_3N_2 has a wider band gap (4.79 eV) in the ultraviolet (UV) region, while Be_3P_2 (1.46 eV) and Be_3As_2 (1.24 eV) have smaller band gaps in the infrared (IR) region. The variation of the

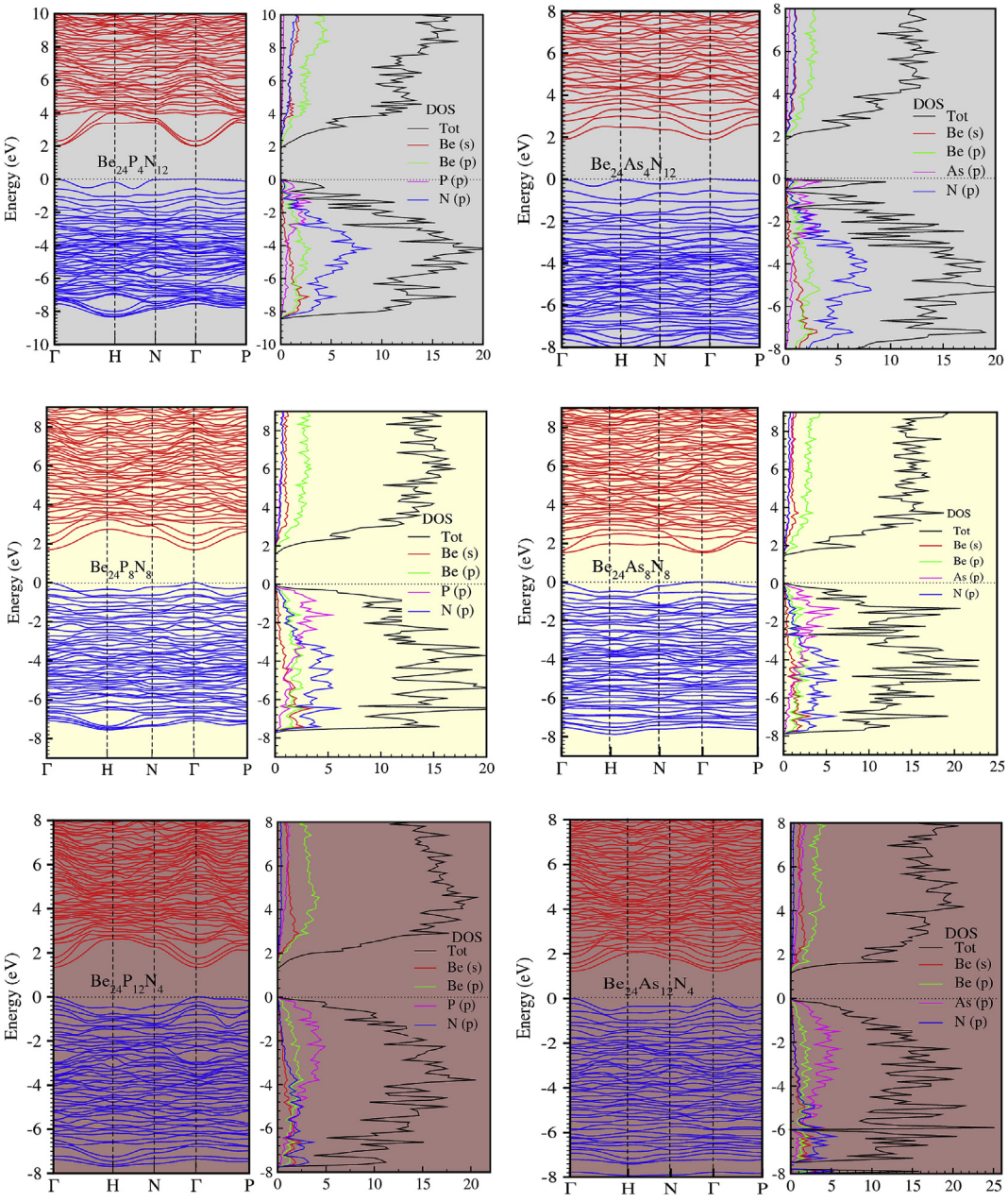

Fig. 4. Band structure and DOS of different $Be_{24}P_xN_{16-x}$ and $Be_{24}As_xN_{16-x}$ ($x = 4, 8, 12$) alloys.

band gap shows that these three semiconductors have potential optical applications in the IR and UV regions of the electromagnetic radiation. It is known that most (90%) of the sun light reaches the earth surface is in the visible range (1.7–3.2 eV). Therefore, it is important to harvest the visible spectra by alloying the parent semiconductors for potential solar energy applications for this purpose, P/As are alloyed in Be_3N_2 semiconductor. The electronic properties are further studied based on density of states (DOS), which clarifies the various electronic contributions of different states. The DOS (total and partial) of pristine Be_3X_2 is depicted in Fig. 2 (right panel). It is seen that the major electronic contribution to the valence band near Fermi level (from −7 eV to 0 eV) originates from the *p*-states of N, P or As. In the conduction band from 0 eV to 8 eV, *p*-states of Be is dominant with minor contributions from Be *s*-states and *p*-states of N, P or As. Electronic transition from the *p*-states of N, P or As in the VB to the *p*-states of Be in the CB is possible. It is also clear from the figure that the band gap of Be_3X_2 (X = N, P or As) becomes smaller as one moves down from N to As in the periodic table.

The band gaps of Be_3X_2 semiconductors and their alloys with different P/As concentrations are shown in Fig. 3. It is seen that the band gap decreases toward the visible light region as one increases the alloying concentration of P (black line) or As (red line). It is also observed that the P/As alloying in Be_3N_2 is more effective in changing the band gap as compared to nitrogen alloying in Be_3P_2 or Be_3As_2. The alloys with higher P/As concentrations (x = 0.25, 0.50 and 0.75) have wider windows of device absorption efficiency than those with lower P/As concentrations (x = 0.06, 0.12 and 0.18).

Fig. 4 (left panel) shows the band structure of the more efficient alloys with different P/As alloying concentrations (x = 0.25, 0.50 and 0.75). It is also noticed that these alloys have small direct band gaps, suggesting potential optoelectronic device applications. For an alloying concentration x = 0.25, the band gaps of $Be_{24}P_4N_{12}$ and $Be_{24}As_4N_{12}$ are 2.01 eV and 1.88 eV, respectively. For an alloying concentration x = 0.50, the band gaps of $Be_{24}P_8N_8$ and $Be_{24}As_8N_8$ are 1.68 eV and 1.52 eV, respectively. For an alloying concentration x = 0.75, the band gaps of $Be_{24}P_{12}N_4$ and $Be_{24}As_{12}N_4$ are 1.33 eV and 1.23 eV, respectively. These alloys have a higher absorption window as compared to the alloys with lower P/As concentrations (x = 0.06, 0.12 and 0.18).

The DOS of $Be_{24}P_xN_{16-x}$ and $Be_{24}As_xN_{16-x}$ with different P or As alloying concentrations (25%, 50% and 75%) are shown in Fig. 4 (right panel). It is interesting to notice that nitrogen *p*-state contribution decreases in the valence band (VB) as one increases the concentration of P or As, while the substitutional P or As *p*-state contribution increases in the VB as well as in the conduction band (CB). In 25% alloying ($Be_{24}P_4N_{12}$ or $Be_{24}As_4N_{12}$), the nitrogen *p*-states are dominant, while the *p*-states of P/As also have some contributions to the VB. As the alloying ratio is increased to 50% ($Be_{24}P_8N_8$ or $Be_{24}As_8N_8$), the host N atom contribution decreases, while the contributions of the substitutional atoms P/As increase in both VB and CB. In higher P or As alloying concentration of 75% ($Be_{24}P_{12}N_4$ or $Be_{24}As_{12}N_4$), an abrupt decrease appears in the *p*-states of N, and the substitutional P or As *p*-states contributions become dominant in the VB as well as in the CB.

3.3. Optical properties and device absorption efficiencies of P/As alloyed Be_3N_2

To study the optical properties of $Be_{24}P_xN_{16-x}$ and $Be_{24}As_xN_{16-x}$ (x = 4, 8, 12, or 16) alloys, we have calculated the imaginary part of the dielectric function (ε_2), which gives a direct measure of the absorption of light spectra. It is known that almost 90% of the sun light reaching the earth surface is below 3.0 eV [30,31]. From Fig. 5a and Fig. 5b, it is seen that the absorption efficiency of pristine $Be_{24}N_{16}$ is very low. $Be_{24}N_{16}$ has a very shallow absorption edge, and the optical band gap is above 5.0 eV, which is not suitable for solar cell applications. To improve the efficiency, we have investigated the alloying effects of phosphorous (P) and arsenic (As). It is obvious from Fig. 5a and b that as the ratio of P/As increases from 0.25 to 0.75, the absorption efficiency of the alloys starts increasing, and the strongest and most uniform absorption is found when the ratio of P/As is equal to 1 (100%). We can also see that the optical band gap starts decreasing and goes to lower energies below 2.0 eV, which is consistent with the electronic band gap values as presented above. For these alloy systems, we can also observe that the absorption edge becomes sharpened as the P/As ratio is increased.

In the case of As alloyed $Be_{24}N_{16}$, we can see that the optical absorption is stronger and the optical band gap goes becomes smaller (below 2 eV) with further sharpened absorption edges as compared to the P alloyed systems. Thus, As alloyed $Be_{24}N_{16}$ is expected to be more suitable for the absorption of infra-red spectral light.

It is known that the imaginary part of the dielectric function gives a direct response of light absorption of a material. For potential solar cell applications we simulate solar devices and calculate their absorption efficiencies. The device absorption efficiencies of pristine and alloy systems are shown in Fig. 6a and Fig. 6b. It is seen that for pristine $Be_{24}N_{16}$ the device absorption efficiency is very low. From Fig. 6a and b, we find that as the ratio of P/As

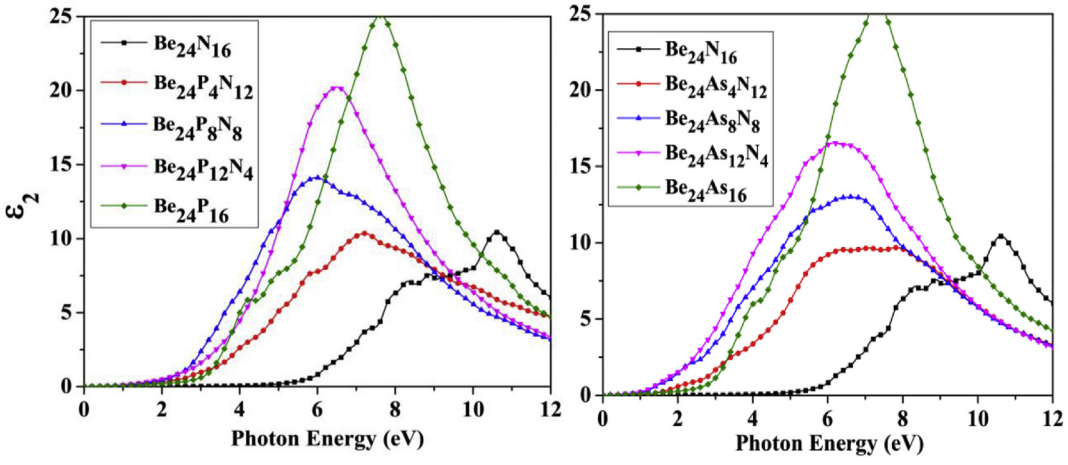

Fig. 5. Imaginary part of the dielectric function (ε_2) for (left) $Be_{24}P_xN_{16-x}$ (x = 4, 8, 12, 16), and (right) $Be_{24}As_xN_{16-x}$ (x = 4, 8, 12, 16).

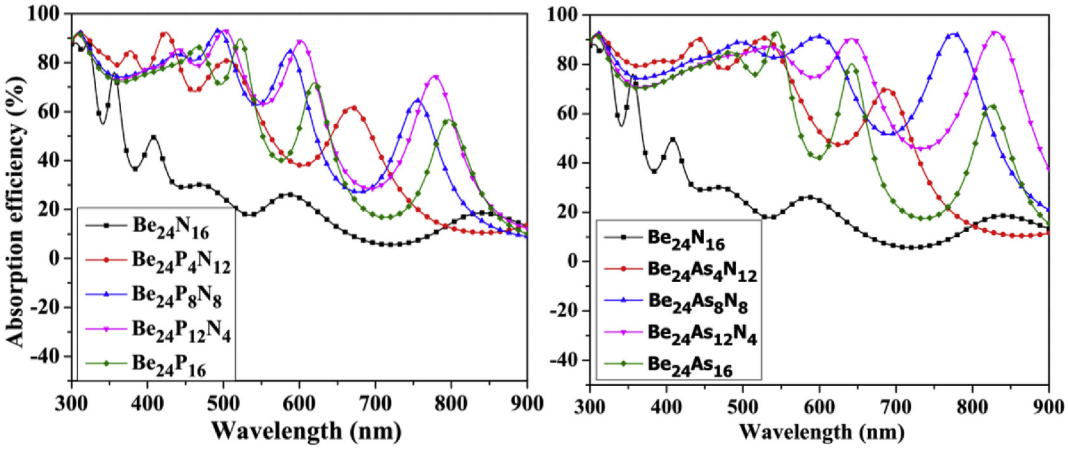

Fig. 6. Absorption efficiency as a function of wavelength of (left) pristine Be_3N_2 and $Be_{24}P_xN_{16-x}$ (x = 4, 8, 12, 16) alloys, and (right) pristine Be_3N_2 and $Be_{24}As_xN_{16-x}$ (x = 4, 8, 12, 16) alloys.

increases from 0.25 to 0.75, the absorption efficiency starts increasing. In the case of P, we find a strong and broad absorption up to 800 nm, while in the case of As, the device absorption efficiency is much stronger in a wider range of wavelength (above 900 nm). It is noted from our calculations that completely replacing N by P or As, the efficiency moves to higher wavelengths, covering almost the entire range of spectral light reaching the earth surface. Hence, it is expected that these newly predicted $Be_{24}P_xN_{16-x}$ or $Be_{24}As_xN_{16-x}$ alloys may have high absorption efficiencies for solar cell applications.

4. Conclusions

The structural, electronic and optical properties of Be_3X_2 and the alloys ($Be_{24}P_xN_{16-x}$ and $Be_{24}As_xN_{16-x}$) have been investigated based on first-principals calculations with-in DFT. Structural parameters of Be_3X_2 compounds obtained in our calculations are consistent with the experimental values. It is found that Be_3N_2 has a wide band gap in the UV region, while Be_3P_2 and Be_3As_2 have smaller band gap values in the IR region. On the other hand, the band gaps of the $Be_{24}P_xN_{16-x}$ and $Be_{24}As_xN_{16-x}$ (x = 4, 8, 12, or 16) alloys are found to be in the range of 1.2–2.01 eV, suitable for the solar absorber applications. For both pristine compounds and their alloys, PDOS calculations show that majority interband electronic transition is between the *p*-states of N, P and As in the VB and the *p*-states of Be in the CB. This interband transition from VB to the unoccupied states in CB results in the major peaks in the optical spectra of the compounds. The device absorption efficiencies of the alloy systems show strong and wide absorption spectra, suggesting potential applications in solar cells.

Acknowledgment

MU is grateful to the Higher Education Commission (HEC) of Pakistan for providing fellowship for his doctoral study. YC acknowledges the support of the HKU Seed Fund for Basic Research under project numbers 201611159149 and 201711159094. The authors are grateful for the research computing facilities offered by ITS, HKU.

References

[1] X. Li, F. Cao, D. Yu, J. Chen, Z. Sun, Y. Shen, Y. Zhu, L. Wang, Y. Wei, Y. Wu, Small 13 (2017) 1603996.
[2] R. Katsube, K. Kazumi, T. Tadokoro, Y. Nose, ACS Appl. Mater. Interfaces 10 (2018) 36102–36107.
[3] C.C. Stoumpos, C.M.M. Soe, H. Tsai, W. Nie, J.-C. Blancon, D.H. Cao, F. Liu, B. Traoré, C. Katan, J. Even, Chemistry 2 (2017) 427–440.
[4] G. Lombardi, F. de Oliveira, M. Teodoro, A. Chiquito, Appl. Phys. Lett. 112 (2018) 193103.
[5] B.D. Homeijer, M. Eichenfield, Google Patents2018.
[6] M. Ullah, G. Murtaza, M. Yaseen, S.A. Khan, J. Alloy. Comp. 728 (2017) 1226–1234.
[7] K. Tsukagoshi, N. Higashi, Google Patents2017.
[8] M. Baig, M. Anis, G. Muley, Optik-Int. J. Light Electron Optics 131 (2017) 165–170.
[9] G.G. Naumis, S. Barraza-Lopez, M. Oliva-Leyva, H. Terrones, Rep. Prog. Phys. 80 (2017), 096501.
[10] A. Mokhtari, H. Akbarzadeh, Phys. B Condens. Matter 324 (2002) 305–311.
[11] K. Joshi, U. Paliwal, J. Phys. Conf. Ser. (2012) 012058. IOP Publishing.
[12] M.G.M. Armanta, A. Reyes-Serrato, Comput. Mater. Sci. 21 (2001) 95–100.
[13] A. Kojima, K. Teshima, Y. Shirai, T. Miyasaka, J. Am. Chem. Soc. 131 (2009) 6050–6051.
[14] V. Ponnambalam, D.T. Morelli, J. Electron. Mater. 42 (2013) 1307–1312.
[15] A. Bhardwaj, D. Misra, RSC Adv. 4 (2014) 34552–34560.
[16] M. Ullah, G. Murtaza, S.M. Ramay, A. Mahmood, Mater. Res. Bull. 91 (2017) 22–30.
[17] G. Soto, J. Dıaz, W. De la Cruz, O. Contreras, M. Moreno, A. Reyes, Mater. Sci. Eng., B 94 (2002) 62–65.
[18] A. Reyes-Serrato, G. Soto, A. Gamietea, M. Farias, J. Phys. Chem. Solids 59 (1998) 743–746.
[19] A. el Maslout, J.-P. Motte, A. Courtois, J. Protas, C. Gleitzer, J. Solid State Chem. 15 (1975) 223–228.
[20] U. Paliwal, K. Joshi, Comput. Mater. Sci. 49 (2010) S268–S271.
[21] O. Reckeweg, C. Lind, A. Simon, F.J. DiSalvo, Z. Naturforsch. B Chem. Sci. 58 (2003) 159–162.
[22] P. Eckerlin, A. Rabenau, Z. Anorg. Allg. Chem. 304 (1960) 218–229.
[23] J. Chang, N. Ge, K. Liu, Phil. Mag. 97 (2017) 2182–2195.
[24] R. Zarmiento-García, A. Reyes-Serrato, M. Xiao, Optik 160 (2018) 109–115.
[25] K. Joshi, U. Paliwal, Phil. Mag. 92 (2012) 1159–1169.
[26] G. Kresse, J. Furthmüller, Comput. Mater. Sci. 6 (1996) 15–50.
[27] J.P. Perdew, K. Burke, M. Ernzerhof, Phys. Rev. Lett. 77 (1996) 3865.
[28] F. Tran, P. Blaha, Phys. Rev. Lett. 102 (2009) 226401.
[29] A.R. Oganov, M. Valle, J. Chem. Phys. 130 (2009) 104504.
[30] R. Ali, G.-J. Hou, Z.-G. Zhu, Q.-B. Yan, Q.-R. Zheng, G. Su, J. Mater. Chem. 6 (2018) 9220–9227.
[31] R. Ali, G.-J. Hou, Z.-G. Zhu, Q.-B. Yan, Q.-R. Zheng, G. Su, Chem. Mater. 30 (2018) 718–728.